MetaHDR: single shot high-dynamic range imaging and sensing using a multifunctional metasurface

CHARLES BROOKSHIRE,[1,†] YUXUAN LIU,[1,†] YUANRUI CHEN,[1] WEI TING CHEN,[2] AND QI GUO[1,*]

[1] *Elmore Family School of Electrical and Computer Engineering, Purdue University, 501 Northwestern Ave, West Lafayette, IN 47906, USA*
[2] *SNOChip INC., 303A College Rd E, Princeton, NJ 08540, USA*
[†] *Co-first authors with equal contribution.*
[*] *qiguo@purdue.edu*

Abstract: We present MetaHDR, which is a single-shot high-dynamic range (HDR) imaging and sensing system using a multifunctional metasurface. The metasurface is capable of splitting an incident beam into multiple focusing beams with different amounts of power, simultaneously forming multiple low dynamic range (LDR) images with distinct irradiance on a photosensor. Then, the LDR images are jointly processed using a gradient-based HDR fusion algorithm, which is shown to be effective in attenuating the residual light artifacts incurred by the metasurface and the lens flare. MetaHDR achieves single-shot HDR photography and videography that increases the dynamic range by at least 50 dB compared to the original dynamic range of the photosensor. It can also perform single-shot HDR sensing, including reflectance calibration and surface curvature estimation of reflective materials. MetaHDR's demonstrated functionalities could be broadly applied in surveillance and security, microscopic imaging, advanced manufacturing, etc.

1. Introduction

High dynamic range (HDR) imaging and sensing have broad applications. From scientific discoveries to national defense, we need cameras and visual sensors that can measure the full visual appearance of the objects of interest. Nowadays, the most widely used photosensors capture RAW images with a bit depth between 12-16 bits [1]. While this allows images to ideally capture scenes with dynamic ranges from approximately 1:4,000 to 1:60,000, the dynamic range of a natural scene can go up to approximately 1:3,000,000 [2]. Therefore, approaches to increase the dynamic range of cameras nowadays are critical and very useful.

One of the most straightforward approaches to achieve HDR imaging without increasing hardware complexity is exposure bracketing [3–5]. This class of methods requires capturing a series of images with a fixed interval of exposure times and then fusing these images together. However, it has to assume the camera and the scene to be static throughout the capture. When there is a relative movement between the camera and the scene during the capture, sophisticated algorithms are required to align and fuse the images together [6–8].

We propose the MetaHDR as a solution to this issue of multi-frame exposure bracketing. MetaHDR is an imaging system that utilizes a metasurface lens to achieve exposure bracketing in a single shot for HDR imaging and sensing. As illustrated in Fig. 1, we design and build a multifunctional metasurface element that divides and focuses the incident light at multiple evenly-spaced positions on the photosensor, each focus containing a select ratio of power incident on the metasurface, mimicking exposure bracketing captures. Therefore, the setup can capture multiple images simultaneously in a single shot, with every photodetector having the same integration time. The core innovation of this work is the design and demonstration of a multifunctional metasurface that works as a multi-beamsplitter with a specific energy distribution and a focusing lens. Multifunctionality is one of the most critical uses of metasurfaces in computational imaging.

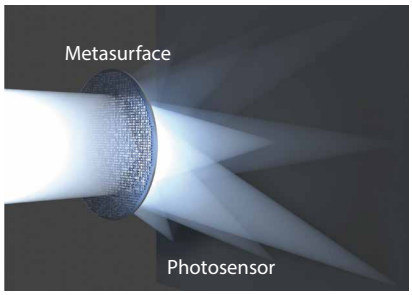

Fig. 1. MetaHDR. The proposed system consists of a multifunctional metasurface that deflects and focuses the incident light at multiple positions on the photosensor, each with a different power, to achieve single-shot exposure bracketing.

There have been multifunctional metasurfaces that exert different modulation functions to the incident wave according to spatial location [9], polarization [10, 11], wavelength [12, 13], incident angle [14], etc. In our experiment, we demonstrate a metasurface designed using a random interleaving approach that simultaneously forms nine images with designed power ratios, which is the highest number of multiplexing achieved by a single piece of metasurface to the best of our knowledge.

We also propose a gradient-based HDR reconstruction algorithm that pairs with the optical design. This algorithm is critical for MetaHDR as we observe inevitable artifacts in the raw measurement, which can corrupt the HDR image generated using traditional HDR reconstruction algorithms, e.g. Debevec and Malik [15]. The artifacts include residual lighting caused by metasurface fabrication defects, which has also been widely witnessed in previous works [9, 13], lens flares on the dim images, and blending of the bright images to the dim images. We show in our experiments that the proposed gradient-based reconstruction algorithm can effectively attenuate these artifacts in the output HDR images.

After the design and fabrication of the metasurface, we assemble a MetaHDR working prototype, a single-shot HDR camera. The prototype operates in a 10nm bandwidth of working wavelength (645nm - 655nm) and can capture HDR images and real-time videos at 500 $\times$ 500-pixel resolution with 50 dB higher dynamic range in addition to the original dynamic range of the photosensor, which is at least 10 dB higher than previous single-shot HDR solutions. In addition, we also demonstrate using MetaHDR to achieve single-shot visual sensing, including surface reflectance calibration and surface curvature estimation of reflective materials from the specularities. Specularities of reflective materials were traditionally treated as unuseful information in computer vision due to the high dynamic range required to capture this information [16–19]. MetaHDR can measure the full intensity profile of a specularity and turn it into useful visual information for material and shape estimation thanks to its extremely high dynamic range, which demonstrates a new potential path for shape reconstruction of reflective materials.

The contribution of this work can be outlined as follows:

- A single-shot HDR imaging and sensing system with a multifunctional metasurface designed using a random interleaving approach;
- A gradient-based HDR reconstruction algorithm paired with the hardware that effectively attenuates various optical artifacts caused by the multifunctional metasurface;
- A working prototype that achieves single-shot HDR imaging and videography with more than 50 dB extra dynamic range compared to the original photosensor, and single-shot surface reflectance and curvature estimation from specularities of reflective materials.

2. Background & Related Work

There are many solutions for generating single-capture HDR images, including both hardware-driven solutions [20–25] and software-driven solutions [26–28]. While both are valuable for furthering HDR capabilities, we choose to review hardware-driven solutions as they are more aligned with the contribution of this work.

Our first categorization of such solutions is exposure mosaicking. These methods involve either manipulating the transmittance [20], polarization [29], or exposure time [21, 22] of groups of pixels, rows of pixels, or individual pixels, to obtain an image encoding multiple exposure times worth of information. These methods are similar to MetaHDR in the idea of reducing the number of captures to generate an HDR image, as they use uniquely capable photosensors, instead of optics, to achieve fine-tuned pixel control [30]. However, the maximum number of single-shot exposure bracketing successfully demonstrated in previous work is limited to at most four, which constrains the highest achievable dynamic range of the system. In this work, MetaHDR demonstrates the simultaneous capture of as many as nine exposure-bracketed images, which increases the dynamic range by at least 10dB compared to previous exposure mosaicking solutions. See Table 1 for details.

The next categorization includes solutions utilizing photon-counting imaging sensors and neuromorphic cameras. Quanta imaging sensors (QIS) and single-photon avalanche diode (SPAD) based imaging sensors are both capable of high-speed photon counting with a low readout noise [31, 32]. Utilizing these properties, multiple exposure images can be generated within a single exposure time. Then, following traditional exposure bracketing reconstruction, HDR images can be generated [23–25]. Neuromorphic cameras, such as event cameras, however, are high frame rate cameras that measure intensity change. While it has been shown asynchronous event detection can be utilized to increase the dynamic range of sensor hardware [33], they tend to be used as a supplementary device in neural network-based solutions for HDR reconstruction [34, 35], or as direct network inputs [28, 36]. This category of HDR solutions requires specialized photosensors and circuitry rather than conventional CMOS cameras. They are complementary to MetaHDR, which is targeted to be compatible with the widely-used camera sensors nowadays. Nevertheless, we list the specifications of some work in this category in Table 1 for information.

3. Metasurface Design and Image Formation Model

The core optical component of MetaHDR is a multifunctional metasurface that serves as a multi-beam splitter and a focusing lens, as shown in Fig. 2. This section describes the design process of the multifunctional metasurface. We model a metasurface, M, as a two-dimensional array of uniform-shape nanocells on a uniform grid G: $M = \{C(m,n)|m,n \in G\}$, where each cell (m,n) is represented by the modulation function $C(m,n)$ it exerts to the traversed wavefront. Specifically, the modulation function $C(m,n)$ exerts a transmittance $T(m,n)$ and phase delay $\phi(m,n)$: $C(m,n) = T(m,n)e^{j\,\phi(m,n)}$, which is determined by the nano-structure of each cell. For this work, we use centered nano-cylinders at a fixed height (Fig. 2b.) This allows us to represent a nanocell's modulation function $C(m,n)$ as a mapping from the nano-cylinder radius r of the cell: $C(m,n) = f(r(m,n))$. We emulate the function $f()$ with a look-up table (LUT) pre-generated using an FDTD solver, where the LUT consists of a set of mappings between nano-cylinder radius r to the modulation function: $\{r_n \rightarrow C_n, n = 1, 2, ..., N\}$. When given a target modulation function $C(m,n)$, we search within the LUT for the nanocells that exhibit the phase delay closest to the specified target modulation function at each position (m,n) and use it as the nanocell shape at (m,n):

$$r(m,n) = \underset{\{r_n, n=1,\cdots,N\}}{arg\,min} \; |\angle C_n - \angle C(m,n)|. \tag{1}$$

Table 1. Comparison of the MetaHDR with recent related work on hardware-driven solutions to HDR imaging. Complementary to previous work that was mostly developed for photography, MetaHDR is targeted to imaging and visual sensing under controlled illumination. It demonstrates the highest dynamic range increase and number of single-shot exposure bracketing under the operating wavelength. Throughout the paper, we report the dynamic range in the unit of dB, which is calculated as $20\log_{10}$ (max_value/min_value) following the tradition of previous work [37]. For the last three rows, we report the extra dynamic range compared to a 16-bit photosensor.

	Key Idea	**Extra Dynamic Range (dB)**	**# Exposure Bracketing**	**Operating Wavelength**	**Capture Procedure**	**Hardware-Specific Signal Processing**	**Raw Resolution**	**Demonstrated Applications**
MetaHDR (Proposed)	Multi-functional Metasurface	55.0	9	10nm FWHM	Single-Shot	Gradient HDR Fusion	570×570	Single-Shot HDR Imaging, Real-Time Video, and Single-Shot Visual Sensing
Xie et al. 2023 [29]	Polarization Mosaicking	28.6	4	Full Visible	Single-Shot	Inconsistency for Polarized Scenes	1224×1024	Single-Shot HDR Photography
Cho et al. 2016 [21]	Exposure Mosaicking	30.1	2	Full Visible	Single-Shot	General HDR Fusion	20MP	Single-Shot HDR Photography
Chi et al. 2023 [38]	Exposure Bracketing	35.9	3	Full Visible	Multi-Shot	General HDR Fusion	24.3MP	Low-light HDR Photography
Qu et al. 2024 [39]	Exposure Mosaicking	36.1	4	Full Visible	Multi-Shot	Demosaicking	6.1MP	HDR Photography
Gnanasambandam et al. 2020 [24]	Photon Counting	40.0	3	Full Visible	QIS Oversampling	QIS Signal Reconstruction	1024×1024	HDR Photography
Ingel et al. 2019 [40]	Photon Counting	23.5	-	Full Visible	SPAD Photon Counting	SPAD Signal Reconstruction	Single Pixel	HDR Photography
Ogi et al. 2021 [37]	Photon Counting	27.6	-	Full Visible	SPAD Photon Counting	SPAD Signal Reconstruction	160x264	HDR Photography
So et al. 2022 [41]	Irradiance Wrapping	36.1	-	Full Visible	Saturation Counting	Irradiance Unwrapping	256x256	HDR photography

Random interleaving. Our goal is to generate a metasurface that unevenly divides the wavefront energy to V focusing locations, allowing for V sub-images to form on the sensor plane. For the prototype we demonstrated in this paper, the number of focusing locations V equals 9. As the number of spatial multiplexing is high and the energy division of each multiplexing is uneven, it is challenging to design the multifunctional metasurface for this work by interleaving the shape profiles of multiple metasurfaces on a regular grid as in Guo et al. [9] and Khorasaninejad et al. [42], which could cause high-order diffraction artifacts in the image. Instead, we develop a random interleaving design procedure for the multifunctional metasurface of this work.

First, we generate the modulation functions $C_i(m,n), i = 1,\cdots,V$ of V *focusing metasurfaces*,

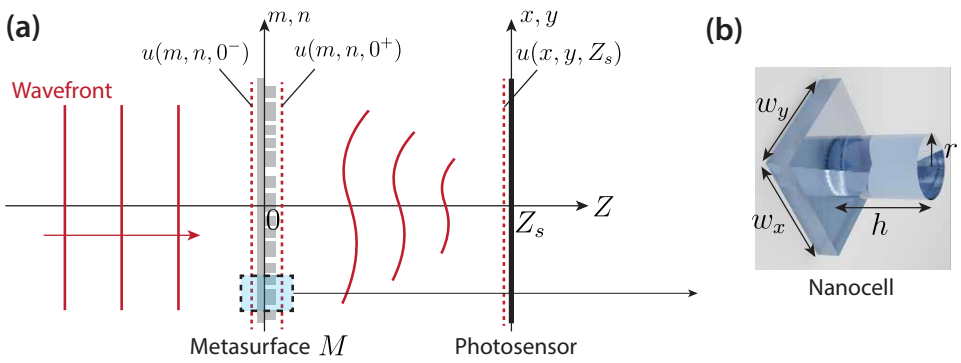

Fig. 2. Metasurface design. (a) A wavefront propagating towards an imaging sensor along the Z-axis. The wavefront interacts with metasurface M, which performs a complex modulation to the traversing wavefront, as characterized by the shape of each nanocell at position (m, n). The modulated wavefront then propagates a distance Z_s to be measured as an image. (b) An individual nanocell of M with a fixed cell size (w_x, w_y) and nano-cylinder height, h. The phase and transmittance applied by this cell are determined by the radius, r, of the nano-cylinder.

via:

$$C_i(m, n) = \exp\left(\frac{j2\pi}{\lambda}\left(\sqrt{(mw_x - x_i)^2 + (nw_y - y_i)^2 + Z_s^2} - Z_s\right)\right), \tag{2}$$

where (x_i, y_i, Z_s) is the coordinate locations we want a fronto-parallel incident plane wave to be focused on the sensor plane, w_x and w_y are the nanocell pitch, and λ is the designed wavelength of the wavefront. Then, we determine the nano-cylinder radius of each cell, $r_i(m, n)$, of the ith focusing metasurface by the nearest neighbor search from the pre-generated LUT via Eq. 1. Finally, we design the *multifunctional metasurface* via random interleaving the V focusing metasurfaces. Denote the shape parameters of the multifunctional metasurface as $r_m(m, n)$. We determine the nano-cylinder radius of each cell (m, n) by randomly picking the nano-cylinder radius from one of the V focusing metasurface shape parameters $r_i(m, n)$ at the same position according to a multinomial distribution:

$$r_m(m, n) = r_i(m, n), i \sim \text{Multinomial}(p_1, p_2, \cdots, p_V), \sum_{i=1}^{V} p_i = 1. \tag{3}$$

The probability of selecting from each focusing metasurface, $p_1, p_2, \cdots, p_V$, determines the portion of the wavefront power that goes to each multiplexed image. We discuss this relationship and how to determine the probabilities, $p_1, p_2, \cdots, p_V$, in the next section.

Image formation model. We treat the scene as a collection of incoherent point sources. For each point source located at $\boldsymbol{X} = [X, Y, Z]$, it emits a coherent wavefront that traverses through the optics. Using the ith focusing metasurface as the optics and assuming paraxial approximation, the image of the point source $\boldsymbol{X}$ is $E(\boldsymbol{X})h_i(x - X/Z, y - Y/Z; Z)$, where $E(\boldsymbol{X})$ denotes the irradiance level received by the photosensor from the point source $\boldsymbol{X}$, and $h_i(x, y; Z)$ represents the point spread function (PSF) of the focusing metasurface $r_i(m, n)$ at object distance Z. The PSFs of the V focusing metasurfaces $h_i(x, y; Z)$ are translational invariant with respect to the index i. Thus, we can simplify the notation of the PSFs:

$$h_i(x - x_i, y - y_i; Z) = h^*(x, y; Z), i = 1, 2, \cdots, V, \tag{4}$$

where we call $h^*(x, y; Z)$ the *ideal PSF* of the focusing metasurfaces. The PSF of the multifunctional metasurface that we design using random interleaving, denoted as $h_m(x, y; Z)$, is related to the ideal PSF $h^*(x, y; Z)$ via the following equation:

$$h_m(x, y; Z) \approx C \cdot \left(\sum_{i=1}^{V} \underbrace{p_i^2 h^*(x - x_i, y - y_i; Z)}_{\text{signal}} + \underbrace{\beta_i(x - x_i + y - y_i)}_{\text{residual}} \right), \tag{5}$$

where the coefficient C is a normalization factor and the term $\beta_i(x - x_i + y - y_i)$ is a background residual light centered at (x_i, y_i). Eq. 5 shows that the PSF of the multifunctional metasurface, $h_m(x, y; Z)$, consists of V multiplexes of the ideal PSFs. The signal term of each multiplex is a translation of the ideal PSF and has an approximate power ratio of Cp_i^2 with respect to the ideal PSF.

When using the multifunctional metasurface as the optics, we denote the *irradiance distribution* on the photosensor from the scene as $E_m(x, y)$:

$$\begin{aligned} E_m(x, y) &= \sum_{\boldsymbol{X}} E(\boldsymbol{X}) h_m(x - X/Z, y - Y/Z; Z), \\ &\propto \sum_{i=1}^{V} \underbrace{p_i^2 E^*(x - x_i, y - y_i)}_{\text{signal}} + \underbrace{b_i(x - x_i, y - y_i)}_{\text{residual}}, \end{aligned} \tag{6}$$

where $E^*(x, y)$ is the *ideal* irradiance distribution on the photosensor under the ideal PSF $h^*(x, y; Z)$. The residual terms in Eq. 5, β_i, become the background irradiance b_i when summing over all points in the scene. By limiting the incident field of view of the optical system, we can constrain the signal term of each multiplex to be separated from each other.

The *full image* measured by the entire photosensor, $I(x, y, t)$, relates to the irradiance distribution according to the noise model of a digital camera [32]:

$$I(x, y, t) = G \cdot \text{Poisson}(\eta \cdot t \cdot E_m(x, y)) + \text{Gauss}(0, \sigma^2), \tag{7}$$

where the coefficients G, η, and t represent gain, quantum efficiency, and exposure time, and σ^2 is the variance of the read noise of the photosensor. We divide the full image panel into V non-overlapping *sub-images*, labeled as $I_i(x, y)$. For simplicity, we skip the variable t in the notation when unnecessary. Each sub-image $I_i(x, y)$ consists of a multiplex of the ideal image. Its coordinate is centered at location (x_i, y_i) in the full image and has a uniform dimension across all sub-images.

Probability selection. We would like to design the power ratio between the ith signal term and i + 1th signal term to be α_i/α_{i+1}. Therefore, according to Eq. 6, the random interleaving probability of each multiplex p_i is:

$$p_i = \frac{\sqrt{\alpha_i}}{\sum_{i=1}^{V} \sqrt{\alpha_i}}, i = 1, 2, \cdots, V. \tag{8}$$

4. Gradient-based HDR Reconstruction

Our HDR reconstruction formulation builds upon Debevec and Malik's work [15] to tackle the imaging artifacts inherent to the proposed system. According to Eq. 6-8, each sub-image $I_i(x, y)$ consists of both the signal and an inevitable background light:

$$I_i(x, y) = G \cdot \text{Poisson}\left(\eta \cdot t \cdot (\alpha_i E^*(x, y) + B_i(x, y))\right) + \text{Gauss}(0, \sigma^2), \tag{9}$$

where the term B_i is a generalized background irradiance that includes all background irradiances b_i in Eq. 6 that blends into the panel of sub-image $I_i(x, y)$:

$$B_i(x, y) = \sum_{j=1}^{V} b_j(x - x_j + x_i, y - x_j + x_i). \tag{10}$$

Based on our experimental observation, we determine it is safe to assume the generalized background irradiance $B_i(x, y)$ to be slowly varying with respect to the spatial coordinates (x, y) compared to the signal. Therefore, the gradient of the sub-images $\partial I_i/\partial x$ and $\partial I_i/\partial y$ only contains the gradient of the signal:

$$\frac{\partial I_i}{\partial x}(x, y) \approx G \cdot \text{Poisson}\left(\eta \cdot t \cdot \alpha_i E_x^*(x, y)\right) + \text{Gauss}(0, \sigma^2). \tag{11}$$

The equation is the same for $\partial I_i/\partial y$. Then, we estimate the spatial gradient of the ideal irradiance distribution E_x^* and $\partial E^*/\partial y$ based on the spatial gradient of the sub-images $\partial I_i/\partial x$ and $\partial I_i/\partial y$ via Debevec and Malik's formulation [15]:

$$\widehat{E_x^*}(x, y) = \underset{E_x^*(x,y)}{\arg\max}\ \Pr\left(E_x^*(x, y)\middle|\frac{\partial I_1}{\partial x}(x, y), \ldots, \frac{\partial I_V}{\partial x}(x, y), \alpha_1, \ldots, \alpha_V\right), \tag{12}$$

and the minimizer is

$$\widehat{E_x^*}(x, y) = \frac{\sum_{i=1}^{V} \alpha_i M_i(x, y)\frac{\partial I_i}{\partial x}(x, y)}{G \cdot \sum_{i=1}^{v} \eta \cdot t \cdot \alpha_i^2 \cdot M_i(x, y)}. \tag{13}$$

The term $M_i(x, y)$ is a binary mask that filters out saturated pixels that could cause inaccurate gradient estimation:

$$M_i(x, y) = \begin{cases} 0 & \text{if a pixel involved in calculating } \dfrac{\partial I_i}{\partial x}(x, y) \text{ is saturated} \\ 1 & \text{otherwise} \end{cases}. \tag{14}$$

The process is the same for estimating E_y^*. Eventually, we can estimate the ideal irradiance distribution from the spatial gradient via Frankot's method [43]:

$$E^*(x, y) = F^{-1}\left(-j\frac{\omega_x F\left(\widehat{E_x^*}(x, y)\right) + \omega_y F\left(\widehat{E_y^*(x, y)}\right)}{\omega_x^2 + \omega_y^2}\right), \tag{15}$$

where F and F^{-1} are Fourier and inverse Fourier transforms.

5. Experimental Results

5.1. Metasurface Design and Fabrication Specifications

We design and fabricate a 1 mm diameter multifunctional metasurface that divides and focuses the incident environmental light into nine low-dynamic range (LDR) sub-images, i.e. $V = 9$, in a 3×3 grid. The arrangement of the nine sub-images is shown in Fig. 6a. The designed power ratio between every two images is two, the designed focal length of the metasurface is 5 cm, and the designed working wavelength is 650 nm. The nanocells of the metasurface are 300 nm $\times$ 300 nm, and the nanopillars are centered α-silicon cylinders of 300 nm height. The nano-cylinder height was selected to make sure that the nanocells can cover a 2π phase delay range. We use the

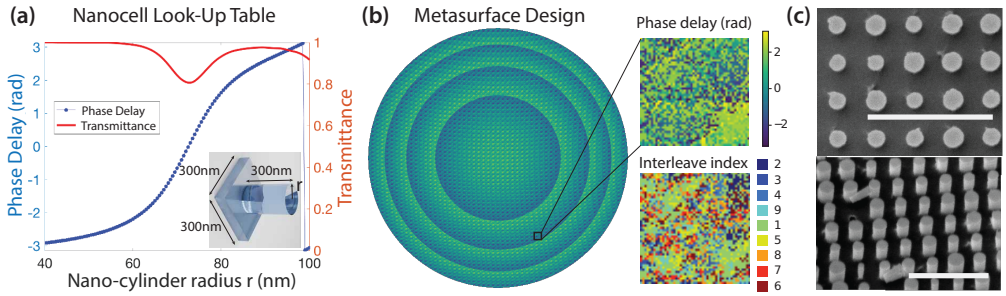

Fig. 3. Details of the metasurface. (a) Phase delay and Transmittance look-up table (LUT) of nanocells with α-Si, cylindrical nanopillar at operating wavelength 650nm that we used. The dimension of each nanocell is 300nm $\times$ 300nm. The nanopillar can be parameterized using the radius r of the cylinder. The nanocells in the LUT cover 2π range of phase delay and achieve a minimum of 0.8 transmittance for the operating wavelength 650nm. (b) The phase delay profile of the designed metasurface. The designed metasurface is 1mm in diameter, with 3335 nanocells in each dimension. The inset figures show the close-up view of the phase delay profiles and the random interleaving indices. (c) Parallel and oblique view SEM image of metasurface nano-structures. Scale bars are $1\mu m$.

Lumerical FDTD simulator to generate the LUT for phase delay and transmittance for the design process (Fig. 3a) and determine the metasurface shape profile following the random interleaving process described in Sec. 3. The phase delay profile and the random interleaving index profile of the designed metasurface are displayed in Fig. 3b.

To verify our design, we estimate the point spread function (PSF) of the designed metasurface by simulating a uniform intensity point source of wavelength 650 nm at a distance of 1 km, sending a spherical wave towards the metasurface. (See Fig. 4a.) In addition to verifying the PSF arrangements, we also examine the average peak signal-to-noise ratio (PSNR) of synthesized images using the PSFs under the noise model in Eq. 7 for various realistic photon levels and noise levels (Fig. 4b.) The simulated images are generated as the convolution of our simulated PSF and a 512×512 8-bit image. The PSNR values remain stable across the photon levels and noise levels, which suggests the sufficient quality of the formed sub-images.

Our metasurface fabrication procedure starts from a bare fused silica glass coated with a 300 nm thick α-Silicon film through plasma-enhanced chemical vapor deposition, Oxford Plasma Pro 100. We then spin coat the silica wafer with a 200 nm thick ARP6200 resist. Next, to help mitigate charging effects and height sensor error during the electron beam lithography process, a 20 nm thick aluminum (Al) layer is deposited onto the sample. Using the electron-beam lithography, EBPG 5150, the sample is patterned with an electron dose of 700uC/cm^2. Afterwards, our sample is soaked in Al etchant type A to remove the Al layer followed by a 90-second development in AR600-546. We deposit a 30-nm-thick Al_2O_3 layer to the sample, followed by lift-off to prepare an etching hard mask. Finally, plasma dry etching was performed using SF_6 and C_4F_8 chemistries [44]. Fig. 3c shows the scanning electron microscope (SEM) photos of the fabricated metasurface nano-structures.

We assemble a MetaHDR prototype using the fabricated metasurface. As visualized in Fig. 5, the prototype can be reconfigured as a microscope using an optional 75mm focal length objective lens. The photosensor of the prototype is monochrome and can capture full images of $2,448 \times 2,048$ pixel resolution.

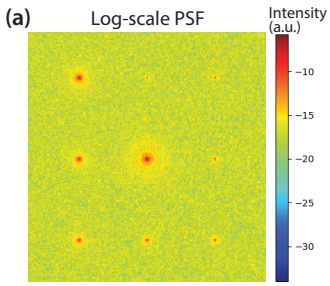

(b)

θ, σ^2	PSNR
$\theta = 10000$ $\sigma^2 = 2$	27.25 dB
$\theta = 5000$ $\sigma^2 = 2$	27.23 dB
$\theta = 2500$ $\sigma^2 = 2$	27.18 dB
$\theta = 10000$ $\sigma^2 = 0$	27.30 dB

Fig. 4. Simulated PSFs and PSNR. (a) The log-scale PSF of the designed metasurface simulated using D-Flat [45]. The metasurface is designed according to the specifications in Sec. 5.1, where it has nine focal points, each with a distinct brightness level. (b) The PSNR of a simulated image with the designed PSF at various noise levels. The exposure value θ is defined as the multiplication of quantum efficiency η and exposure time t, and σ is the read noise level, both according to Eq. 7.

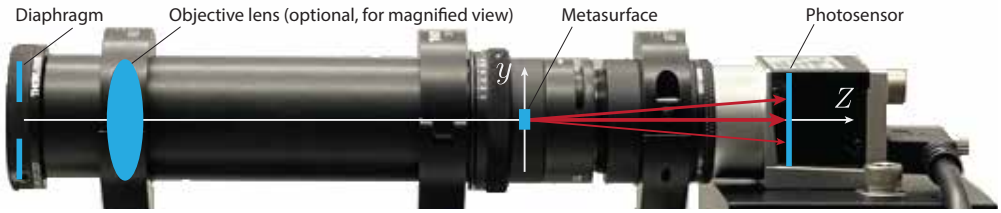

Fig. 5. MetaHDR Prototype. The 1 mm diameter metasurface is mounted 5 cm from the image sensor. We include a diaphragm with an additional lens tubing to constrain the field of view so that the nine sub-images have minimal overlap. The prototype can optionally insert a second objective lens for the magnified view and improved light efficiency. The photosensor we use is the Basler ace acA2440-35um with 5M pixels.

5.2. Calibration

The calibration of MetaHDR involves two steps: geometric alignment and contrast registration. The geometric alignment determines a homography H_{ij} between every pair of sub-images $I_i(x, y)$ and $I_j(x, y)$. We align all sub-images to a reference sub-image through perspective warping using the calibrated homographies. Fig. 6b shows the homography estimation process, where we image a calibration target using MetaHDR and detect corresponding key points between sub-images to calculate the homography. The detailed process is in the supplementary material.

The contrast registration estimates the power ratio of the signal term of each sub-image, α_i, in Eq. 9. We use MetaHDR to capture the V sub-images of a static, textured pattern. For each sub-image, $I_i(x, y)$, we select the exposure time t_i so that the specific sub-image is unsaturated and properly exposed. We estimate the unnormalized power ratio $\tilde{\alpha}_i$ of the ith sub-image by registering its spatial gradient with that of a reference sub-image:

$$\tilde{\alpha}_i = \frac{t_2}{t_i} \cdot \frac{\sum_{x,y} \|\nabla I_i(x, y)\|^2}{\sum_{x,y} \nabla I_i(x, y) \cdot \nabla I_2(x, y)}, \tag{16}$$

where $\nabla I_i = [\partial I_i/\partial x, \partial I_i/\partial y]^T$. In our experiment, we use $I_2(x, y)$ as the reference sub-image. We then calculate the normalized power ratio α_i so that it reflects the power ratio of each sub-image with respect to the ideal image. Details of the contrast registration are described in the supplementary material. Table 2 lists the estimated normalized power ratios α_i of MetaHDR. The power ratio of adjacent images is approximately two, which is consistent with our design.

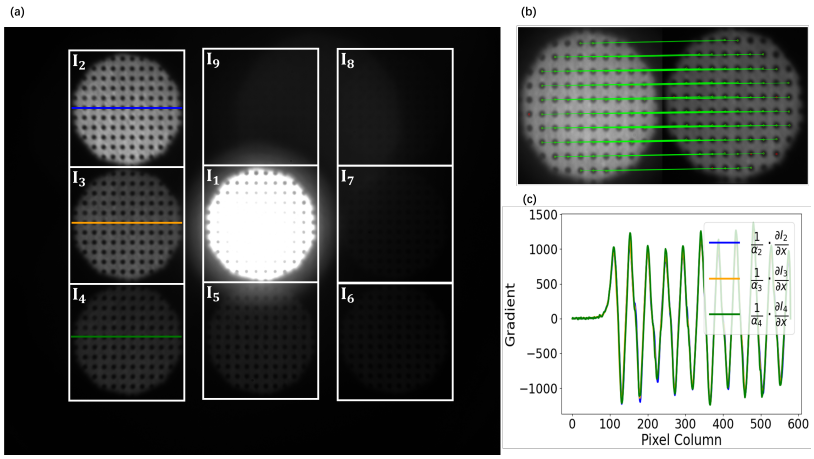

Fig. 6. Geometric alignment and contrast alignment. (a) Sample full image of the calibration target with sub-image division. (b) Key point detection between I_2 and I_3 for geometric alignment. (c) Cross-section of the sample sub-image spatial gradient after the calibration. After dividing the corresponding power ratios, the intensity profiles of the spatial gradient closely match each other.

The power ratio between the brightest and dimmest images is $\alpha_1/\alpha_9 = 562.5$, which means that the system can achieve 562.5 times or 55.00 dB extra dynamic range than that of the photosensor. To examine the quality of the contrast registration, we also visualize the cross-section of contrast-registered sub-image spatial gradient $(1/\alpha_i) \cdot \partial I_i/\partial x$ in Fig. 6c. Qualitatively, the spatial gradient of each sub-image is shown to be accurately aligned after their corresponding power ratios are canceled.

Table 2. Calibrated power ratio of each sub-image of MetaHDR. The power ratio we report in this table is the intensity ratio of the sub-image over the ideal image. The power ratios between most adjacent sub-images, α_i and α_{i+1}, have a proportion of around 2, which is consistent with our design. The total power ratio among the nine images, α_1/α_9, is 562.5. Therefore, the MetaHDR prototype can maximally increase the dynamic range by a ratio of 562.5, or 55.00 dB, via exposure bracketing.

Power ratio	α_1	α_2	α_3	α_4	α_5	α_6	α_7	α_8	α_9
MetaHDR	0.36	0.14	0.073	0.034	0.019	0.0089	0.0045	0.0019	0.00064

5.3. HDR Imaging Results

Without the objective lens, the prototype can capture sharp images of 10 cm × 10 cm dimension objects at 2 m away, and with the objective lens, the prototype can image 2.5 mm × 2.5 mm objects placed at around 3 cm away from the diaphragm. The reconstructed HDR image is of 570 × 570 pixel resolution. Fig. 7 shows sample HDR images taken using the prototype without (Fig. 7a-c) and with (Fig. 7d-e) the objective lens. We demonstrate that MetaHDR can simultaneously record the radiance profile of an extremely bright incandescent light bulb and see the dark textured plane in the scene (Fig. 7a). It can also record HDR images of dynamic scenes such as the flame (Fig. 7c).

Fig. 8 shows a qualitative comparison of the HDR image reconstructed using the gradient-based fusion method vs. the method of Debevec and Malik [15]. The gradient-based method effectively

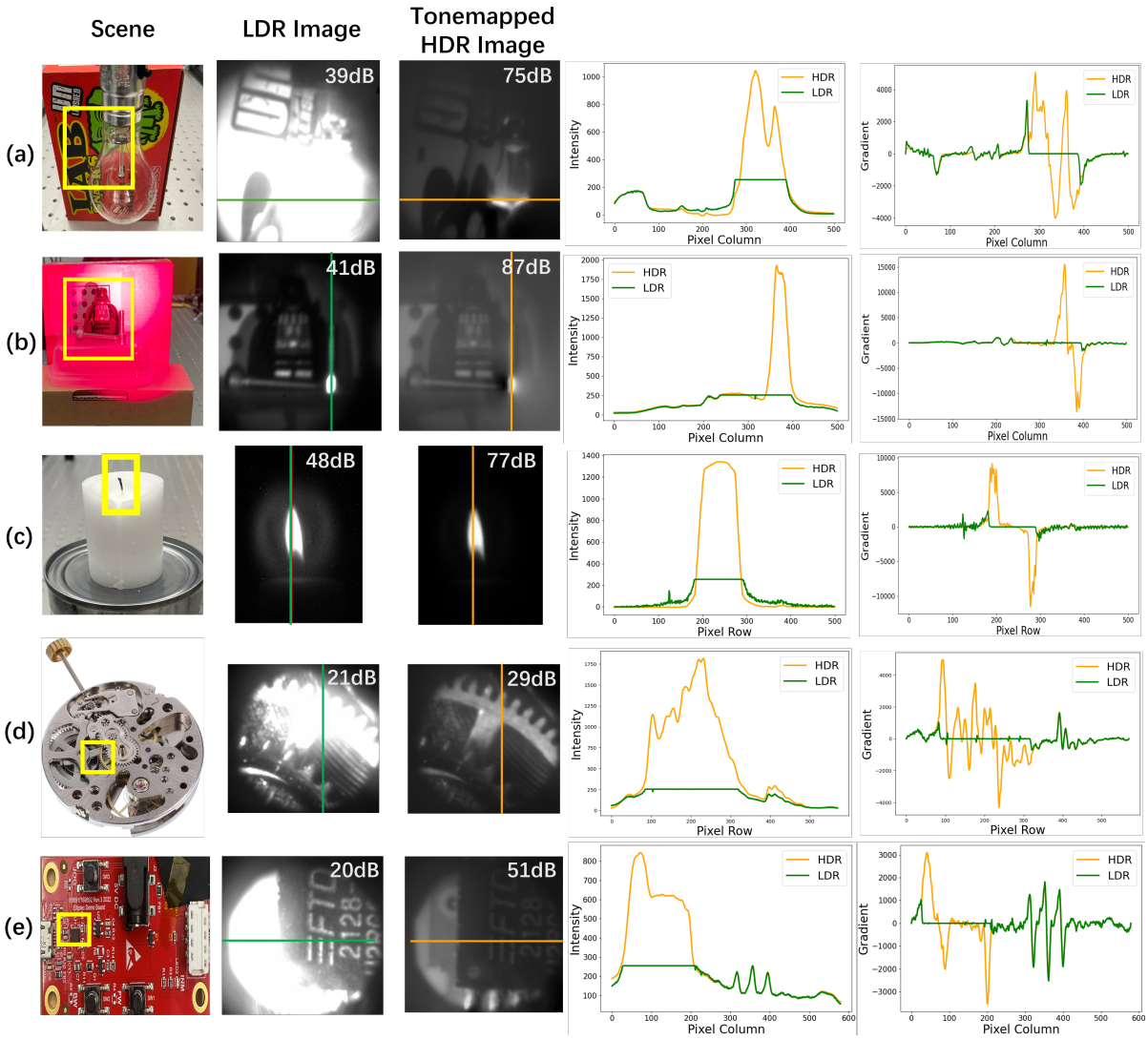

Fig. 7. Single-shot HDR imaging results captured using MetaHDR. Rows (a) - (e) represent different scenes. The first column is a photo of the imaged scene with a bounding box indicating the area captured by MetaHDR. The second column is the brightest LDR sub-image captured for each scene. The numbers on the top left are the dynamic range of the images. The third column is the tonemapped HDR image reconstructed using the gradient-based fusion method, with the dynamic range of the image listed on the top left. All dynamic range values are calculated as the maximum pixel value divided by the minimum pixel value in the field of view. The fourth and fifth columns are cross-sections of the intensity and spatial gradients of sub-image (LDR) and reconstructed HDR images, which clearly show the saturation of the LDR images. Scenes (a-c) and (d-e) are captured without and with the objective lens, respectively. With the objective lens, MetaHDR becomes a microscope with a 2.5 mm $\times$ 2.5 mm field of view and a resolution of around 20 um.

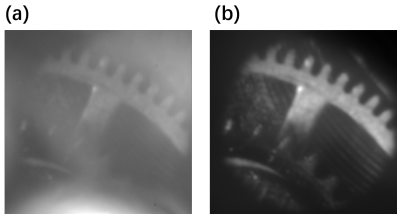

Fig. 8. Artifacts attenuation via the gradient-based HDR fusion. (a) Intensity-based HDR fusion with tonemapping [15]. (b) Gradient-based HDR fusion with tonemapping. The gradient approach clearly attenuates various artifacts, including the background light and the blending of neighboring sub-images.

removes the optical artifacts caused by residual lights.

Besides HDR images, the setup can also capture HDR videos in real-time. In the supplementary material, we demonstrate two HDR videos of moving objects captured using and without using the objective lens.

Light efficiency comparison. MetaHDR is complementary to the existing HDR solutions that use pixel mosaicking to achieve single-shot exposure bracketing, including using mosaicked optical filter arrays [20, 29], mosaicked shutter times [21]. These exposure mosaicking methods can operate in a broader wavelength than MetaHDR. Meanwhile, for applications that only require a single wavelength, MetaHDR can achieve a higher light efficiency than exposure mosaicking, as the latter solution discards a portion of incident light by the filter arrays or the reduced shutter times during a single capture. Table 3 shows the estimated light efficiency of the MetaHDR prototype and an ideal nine-exposure mosaicking imager. We also assess the HDR quality of both solutions under the estimated light efficiency. Details of the light efficiency estimation and HDR quality comparison are in the supplementary material. In our comparison, MetaHDR demonstrates two times higher light efficiency than exposure mosaicking, and 6dB higher PSNR in HDR reconstruction according to the estimated light efficiency.

5.4. HDR Sensing Results

We also explore MetaHDR's single-shot HDR capability to improve traditional computer vision solutions. Specifically, we exploit MetaHDR to capture the full intensity profile of specularities on reflective materials in a single shot and use it to estimate the material properties, including surface reflectance or local curvature.

Single-shot surface reflectance calibration. First, we demonstrate using MetaHDR to calibrate the surface reflectance of glossy materials, such as metals, in a single shot. Traditionally, this

Table 3. Comparison between MetaHDR and a hypothesized 9-exposure mosaicking HDR imager. We estimate the light efficiencies of both methods and analyze the HDR image quality generated using the corresponding light efficiencies for both methods. The results show clear differences in HDR reconstruction quality on all three metrics caused by differences in the light efficiency of both solutions. A detailed description of the comparison process is described in the supplementary material.

	Hypothesized Light Efficiency	MSE ↓	PSNR (dB) ↑	SSIM ↑
MetaHDR Prototype	53.7%	0.0684	28.784	0.4761
Hypothesized Exposure Mosaicking	22.2%	0.3584	22.747	0.2454

task was only demonstrated using multi-shots exposure bracketing to capture the full intensity profile of the specularities [46]. We place a precision ball with a known radius r in front of the MetaHDR. As shown in Fig. 9a, using a background light to locate the contour of the precision ball, we can estimate the 3D position $\mathbf{X}$ and surface normal $\mathbf{N}$ of the point on the ball that corresponds to every pixel (x, y) in the captured image. Then, we fix a directional light onto the ball, which will create a specularity on the surface (Fig. 9a). After reconstructing the HDR irradiance map of the scene $E^*(x, y)$, we can estimate the lighting direction $\mathbf{L}$ via $\mathbf{L} = 2\mathbf{N}_0 - \mathbf{V}$, where vector $\mathbf{N}_0$ is the surface normal of the point that corresponds to the brightest pixel in the irradiance map and vector $\mathbf{V}$ is the viewing direction. We assume orthographic projection and set $\mathbf{V} = [0, 0, 1]^T$. Finally, using the HDR irradiance map, we can fit the surface reflectance model through the following optimization:

$$\widehat{\mathbf{k}} = \arg\min_{\mathbf{k}} \sum_{x,y} \left(E^*(x, y) - \rho L(\mathbf{L}, \mathbf{V}, \mathbf{N}(x, y); \mathbf{k})\right)^2, \tag{17}$$

where the coefficient ρ is the normalization parameter and $L(\mathbf{L}, \mathbf{V}, \mathbf{N}; \mathbf{k}))$ is the parameterized surface reflectance model with parameters $\mathbf{k}$. We adopt the Phong reflectance model [47], which has been broadly used for modeling the reflectance of glossy materials:

$$L(\mathbf{L}, \mathbf{V}, \mathbf{N}; \mathbf{k} = \{N, K_s, K_d, K_a\}) = K_s \cdot (\max(\mathbf{V} \cdot \mathbf{R}, 0))^N + K_d \cdot (\max(\mathbf{N} \cdot \mathbf{R}, 0)) + K_a. \tag{18}$$

The coefficient N describes the reflectivity of the material, and coefficients K_s, K_d, and K_a are the weights of specular, diffuse, and ambient components of the reflection.

We use MetaHDR to calibrate the surface reflectance of multiple glossy materials, including stainless steel, tungsten carbide, and brass. Part of the results are shown in Fig. 9, and the rest are in the supplementary material. We plot the calibrated reflectance model in the form of bi-direction reflectance distribution functions (BRDFs) in Fig. 9b-c. To verify the accuracy of the reflectance calibration, we render the image of the precision ball from a novel lighting direction and compare it with the real measurements. As shown in Fig. 9e, the cross-section of the rendered image and the real measurement closely match each other. We also show a rendered image of the calibrated material under custom environments in Fig. 9f, as rendering is a classic application of surface reflectance calibration. Although the surface reflectance is measured in a single wavelength in this experiment, the specular reflectance, which consists of the most power, is shown to be approximately uniform across the visible spectral band [48].

Single-shot surface curvature estimation. We also demonstrate using MetaHDR to simultaneously estimate the lighting direction and the surface curvature of the material from the specularity of a reflective object, given its surface reflectance model. Traditionally, estimating the shape of reflective materials has been a challenging task in computer vision, which involves using rigorously calibrated diffuse illumination to avoid specularities and perform photometric stereo or shape from shading [50, 51], or only using the unsaturated pixels in the low dynamic range images of the object [16–18]. Using MetaHDR, we can directly measure the local curvature of the object at the specularity in a single shot without knowledge of the light source and with a weak prior of the shape.

In our experiment, we assume the distance map of the local surface at the specularity follows the quadratic function, as used in Xiong et al. [52]:

$$Z(x, y; \mathbf{a}) = a_1(x - x_0)^2 + a_2(y - y_0)^2 + a_3(x - x_0)(y - y_0) + a_4(x - x_0) + a_5(y - y_0), \tag{19}$$

where Z is the distance of the point corresponding to pixel (x, y), the vector $\mathbf{a} = [a_1, \cdots, a_5]^T$ is the parameterization of the shape, with $[a_1, \cdots, a_3]$ indicating the curvature, and (x_0, y_0) are

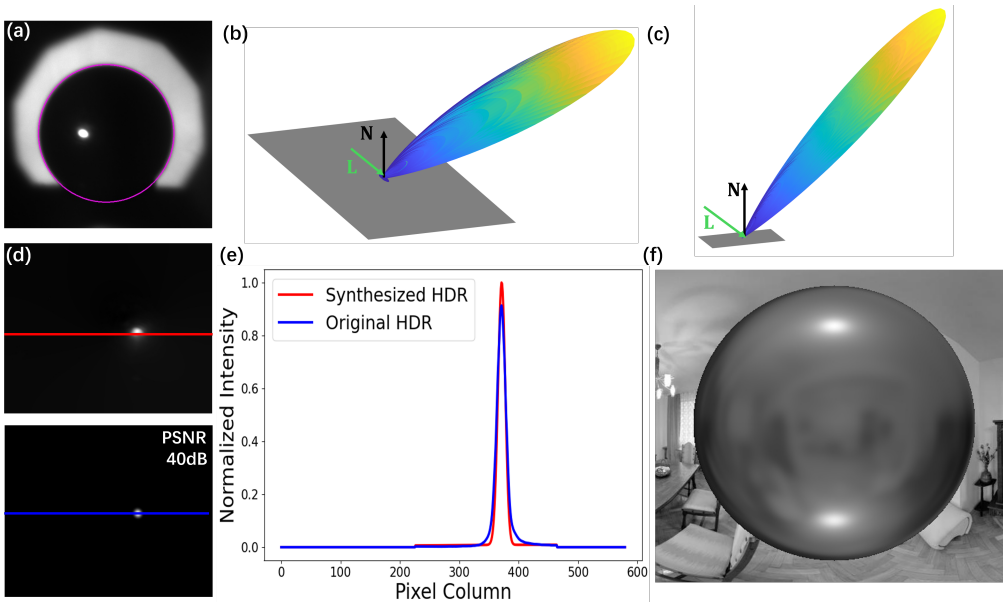

Fig. 9. Single-shot surface reflectance calibration from specularities. (a) By using a precision ball as the target, we can determine the 3D position and surface normal direction of every pixel from the circular contour of the ball. (b-c) The calibrated reflectance models are visualized in the form of bi-directional radiance distribution functions (BRDF) for stainless steel (b) and tungsten carbide (c). (d) We compare the measured (upper) and rendered (lower) HDR images of the stainless steel precision ball under a different illumination direction. The PSNR of the rendering is 40 dB. (e) We visualize the cross-section of the measured and rendered HDR irradiance map, which is shown to closely match each other. (f) Rendering of a stainless steel precision ball in a custom environment sampled from the SUN360 dataset [49]. Additional results are in the supplementary material.

the pixels with the highest intensity in the specularity. The shape of the local surface at the specularity and the lighting direction $\mathbf{L}$ can be estimated via the following optimization problem:

$$\widehat{\mathbf{a}}, \widehat{\mathbf{L}} = \arg\min_{\mathbf{a},\mathbf{L}} \sum_{x,y} \left(E^*(x,y) - \rho L(\mathbf{L}, \mathbf{V}, \mathbf{N}(x,y;\mathbf{a}); \mathbf{k})\right)^2 . \tag{20}$$

where the vector $\mathbf{V}$ is the viewing direction and $\mathbf{N}$ is the surface normal direction. To avoid ambiguities in the solution, we initialize the second-order coefficients $a_1, \cdots, a_3$ as negative values based on the prior knowledge that the shape of the local surface is convex. As shown in Fig. 10. MetaHDR successfully predicts the 3D shape of the two stainless steel surfaces at the specularity and the lighting direction in a single shot with a small error. See supplementary material for more results.

6. Discussions and Limitations

MetaHDR is an example of integrating nanophotonics and computer vision to advance imaging and visual sensing. In this work, we demonstrate that this integration can produce a new HDR solution, MetaHDR, that achieves the highest dynamic range increase compared to previous methods and demonstrates single-shot imaging and visual sensing. MetaHDR could have broad applications in surveillance and security, microscopic imaging, advanced manufacturing, etc.

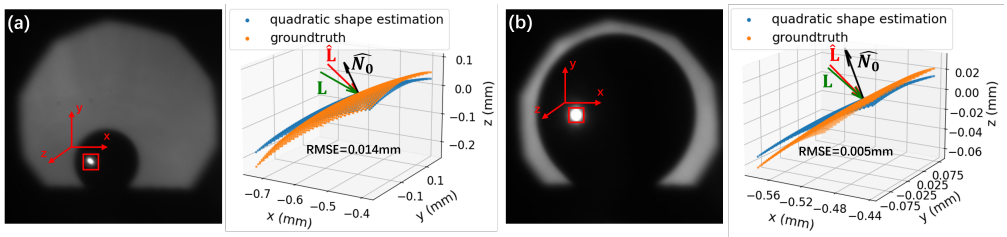

Fig. 10. Single-shot surface curvature estimation from specularities. We use the surface reflectance model measured in advance from a 2 mm stainless steel precision ball to recover the local curvature of unknown surfaces of the same material at the specularities (red patches) and the lighting direction. The unknown surfaces are precision balls with (a) 1 mm and (b) 2.5 mm diameters so that we have access to the ground truth surface shape and lighting direction. The reconstruction is purely based on the intensity profile of the specularity within each local patch and a weak prior knowledge that the surface is convex for initialization of coefficients $\mathbf{a}$. We plot the reconstructed surfaces and overlay them with ground truths. We also visualize the estimated lighting direction $\widehat{\mathbf{L}}$, the estimated surface normal of the brightest pixel $\widehat{\mathbf{N}_0}$, and the ground truth lighting direction $\mathbf{L}$. The average error of the estimated lighting direction $\widehat{\mathbf{L}}$ is 9.5°. Additional results are in the supplementary material.

A potential limitation of the current system is the relatively small deflection angles of off-axis sub-images and the small numerical aperture of the metasurface in the prototype. These problems can be resolved by improving the design of the multifunctional metasurface.

Funding. Samsung Research America Global Research Outreach (GRO) 2023.

Acknowledgement. The authors want to thank Professors Gregory Buzzard, Stanley Chan, Song Zhang, and Michael Zoltowski for their helpful discussions.

Disclosures. The authors declare no conflict of interest.

Data availability. Data underlying the results presented in this paper are not publicly available at this time but may be obtained from the authors upon reasonable request.

Supplemental Document. See Supplementary Video for the HDR videography performance of the system.

References

1. T. Photometrics, "Bit depth, full well, and dynamic range - learn," (2022).
2. A. Grimaldi, D. Kane, and M. Bertalmio, "Statistics of natural images as a function of dynamic range," J. Vis. **19**, 13–13 (2019).
3. N. Barakat, A. N. Hone, and T. E. Darcie, "Minimal-bracketing sets for high-dynamic-range image capture," Trans. Img. Proc. **17**, 1864–1875 (2008).
4. R. Pourreza-Shahri and N. Kehtarnavaz, "Exposure bracketing via automatic exposure selection," in *2015 IEEE International Conference on Image Processing (ICIP),* (2015), pp. 320–323.
5. K. Hirakawa and P. J. Wolfe, "Optimal exposure control for high dynamic range imaging," in *2010 IEEE International Conference on Image Processing,* (2010), pp. 3137–3140.
6. O. Gallo and P. Sen, *Stack-Based Algorithms for HDR Capture and Reconstruction* (2016), pp. 85–119.
7. S. Catley-Chandar, T. Tanay, L. Vandroux, *et al.*, "Flexhdr: Modeling alignment and exposure uncertainties for flexible hdr imaging," IEEE Trans. on Image Process. **31**, 5923–5935 (2022).
8. S. Wu, J. Xu, Y.-W. Tai, and C.-K. Tang, "End-to-end deep hdr imaging with large foreground motions," in *European Conference on Computer Vision,* vol. 1 (2018).
9. Q. Guo, Z. Shi, Y.-W. Huang, *et al.*, "Compact single-shot metalens depth sensors inspired by eyes of jumping spiders," Proc. National Acad. Sci. **116**, 22959–22965 (2019).
10. D. Hazineh, S. W. D. Lim, Q. Guo, *et al.*, "Polarization multi-image synthesis with birefringent metasurfaces," in *2023 IEEE International Conference on Computational Photography (ICCP),* (IEEE, 2023), pp. 1–12.

11. N. A. Rubin, Z. Shi, and F. Capasso, "Polarization in diffractive optics and metasurfaces," Adv. Opt. Photonics **13**, 836–970 (2021).
12. E. Arbabi, A. Arbabi, S. M. Kamali, *et al.*, "Multiwavelength metasurfaces through spatial multiplexing," Sci. reports **6**, 32803 (2016).
13. Z. Shi, M. Khorasaninejad, Y.-W. Huang, *et al.*, "Single-layer metasurface with controllable multiwavelength functions," Nano letters **18**, 2420–2427 (2018).
14. A. M. Shaltout, V. M. Shalaev, and M. L. Brongersma, "Spatiotemporal light control with active metasurfaces," Science **364**, eaat3100 (2019).
15. P. E. Debevec and J. Malik, "Recovering high dynamic range radiance maps from photographs," SIGGRAPH 97 (1997).
16. K. E. Torrance and E. M. Sparrow, "Theory for off-specular reflection from roughened surfaces," Josa **57**, 1105–1114 (1967).
17. G.-h. Liu, X.-Y. Liu, and Q.-Y. Feng, "3d shape measurement of objects with high dynamic range of surface reflectivity," Appl. optics **50**, 4557–4565 (2011).
18. J. Wang and K. J. Dana, "Relief texture from specularities," IEEE Trans. on pattern analysis machine intelligence **28**, 446–457 (2006).
19. F. Tong and B. V. Funt, "Removing specularities from color images for shape from shading," in *Computer Vision and Shape Recognition,* (World Scientific, 1989), pp. 273–290.
20. S. Nayar and T. Mitsunaga, "High dynamic range imaging: spatially varying pixel exposures," in *Proceedings IEEE Conference on Computer Vision and Pattern Recognition. CVPR 2000 (Cat. No.PR00662),* vol. 1 (2000), pp. 472–479 vol.1.
21. H. Cho, S. J. Kim, and S. Lee, "Single-shot high dynamic range imaging using coded electronic shutter," Comput. Graph. Forum **33**, 329–338 (2014).
22. J. N. P. Martel, L. K. Müller, S. J. Carey, and P. Dudek, "Parallel hdr tone mapping and auto-focus on a cellular processor array vision chip," in *2016 IEEE International Symposium on Circuits and Systems (ISCAS),* (2016), pp. 1430–1433.
23. N. A. Dutton, T. Al Abbas, I. Gyongy, *et al.*, "High dynamic range imaging at the quantum limit with single photon avalanche diode-based image sensors," Sensors **18** (2018).
24. A. Gnanasambandam and S. H. Chan, "Hdr imaging with quanta image sensors: Theoretical limits and optimal reconstruction," IEEE Trans. on Comput. Imaging **6**, 1571–1585 (2020).
25. A. Ingle, T. Seets, M. Buttafava, *et al.*, "Passive inter-photon imaging," (2021).
26. C. A. Metzler, H. Ikoma, Y. Peng, and G. Wetzstein, "Deep optics for single-shot high-dynamic-range imaging," (2019).
27. G. Eilertsen, J. Kronander, G. Denes, *et al.*, "Hdr image reconstruction from a single exposure using deep cnns," ACM Trans. Graph. **36** (2017).
28. M. Mostafavi, L. Wang, and K.-J. Yoon, "Learning to reconstruct hdr images from events, with applications to depth and flow prediction," Int. J. Comput. Vis. **129**, 900–920 (2021).
29. M. Xie, M. Chan, and C. Metzler, "Snapshot high dynamic range imaging with a polarization camera," arXiv preprint arXiv:2308.08094 (2023).
30. S. Carey, A. Lopich, D. Barr, *et al.*, "A 100,000 fps vision sensor with embedded 535gops/w 256×256 simd processor array," (2013), pp. C182–C183.
31. J. Buchholz, J. Krieger, C. Bruschini, *et al.*, "Widefield high frame rate single-photon spad imagers for spim-fcs," Biophys. J. **114** (2018).
32. S. H. Chan, "What does a one-bit quanta image sensor offer?" (2022).
33. J. A. Lenero-Bardallo, R. Carmona-Galán, and Á. Rodríguez-Vázquez, "A high dynamic range image sensor with linear response based on asynchronous event detection," in *2015 European Conference on Circuit Theory and Design (ECCTD),* (IEEE, 2015), pp. 1–4.
34. N. Messikommer, S. Georgoulis, D. Gehrig, *et al.*, "Multi-bracket high dynamic range imaging with event cameras," in *Proceedings of the IEEE/CVF Conference on Computer Vision and Pattern Recognition (CVPR) Workshops,* (2022), pp. 547–557.
35. R. Shaw, S. Catley-Chandar, A. Leonardis, and E. Perez-Pellitero, "Hdr reconstruction from bracketed exposures and events," (2022).
36. H. Rebecq, R. Ranftl, V. Koltun, and D. Scaramuzza, "High speed and high dynamic range video with an event camera," (2019).
37. J. Ogi, T. Takatsuka, K. Hizu, *et al.*, "A 124-db dynamic-range spad photon-counting image sensor using subframe sampling and extrapolating photon count," IEEE J. Solid-State Circuits **56**, 3220–3227 (2021).
38. Y. Chi, X. Zhang, and S. H. Chan, "Hdr imaging with spatially varying signal-to-noise ratios," in *Proceedings of the IEEE/CVF Conference on Computer Vision and Pattern Recognition,* (2023), pp. 5724–5734.
39. X. Qu, Y. Chi, and S. H. Chan, "Spatially varying exposure with 2-by-2 multiplexing: Optimality and universality," IEEE Trans. on Comput. Imaging (2024).
40. A. Ingle, A. Velten, and M. Gupta, "High flux passive imaging with single-photon sensors," in *Proceedings of the IEEE/CVF Conference on Computer Vision and Pattern Recognition,* (2019), pp. 6760–6769.
41. H. M. So, J. N. Martel, G. Wetzstein, and P. Dudek, "Mantissacam: Learning snapshot high-dynamic-range imaging

with perceptually-based in-pixel irradiance encoding," in *2022 IEEE International Conference on Computational Photography (ICCP),* (IEEE, 2022), pp. 1–12.
42. M. Khorasaninejad, W. Chen, A. Zhu, *et al.*, "Multispectral chiral imaging with a metalens," Nano letters **16**, 4595–4600 (2016).
43. R. T. Frankot and R. Chellappa, "A method for enforcing integrability in shape from shading algorithms," IEEE Trans. on pattern analysis machine intelligence **10**, 439–451 (1988).
44. M. Henry, S. Walavalkar, A. Homyk, and A. Scherer, "Alumina etch masks for fabrication of high-aspect-ratio silicon micropillars and nanopillars," Nanotechnology **20**, 255305 (2009).
45. D. S. Hazineh, S. W. D. Lim, Z. Shi, *et al.*, "D-flat: A differentiable flat-optics framework for end-to-end metasurface visual sensor design," (2022).
46. W. Matusik, H. Pfister, M. Brand, and L. McMillan, "Efficient isotropic brdf measurement," in *Proceedings of the 14th Eurographics workshop on Rendering,* (2003), pp. 241–247.
47. B. T. Phong, "Illumination for computer generated pictures," in *Seminal graphics: pioneering efforts that shaped the field,* (1998), pp. 95–101.
48. A. Ferrero, J. Campos, A. M. Rabal, *et al.*, "Principal components analysis on the spectral bidirectional reflectance distribution function of ceramic colour standards," Opt. Express **19**, 19199–19211 (2011).
49. J. Xiao, K. A. Ehinger, A. Oliva, and A. Torralba, "Recognizing scene viewpoint using panoramic place representation," in *2012 IEEE Conference on Computer Vision and Pattern Recognition,* (IEEE, 2012), pp. 2695–2702.
50. K. Ikeuchi, "Determining surface orientations of specular surfaces by using the photometric stereo method," IEEE Trans. on Pattern Anal. Mach. Intell. pp. 661–669 (1981).
51. Y. Adato, Y. Vasilyev, T. Zickler, and O. Ben-Shahar, "Shape from specular flow," IEEE transactions on pattern analysis machine intelligence **32**, 2054–2070 (2010).
52. Y. Xiong, A. Chakrabarti, R. Basri, *et al.*, "From shading to local shape," IEEE transactions on pattern analysis machine intelligence **37**, 67–79 (2014).